MR Microscopy of Transgenic Mice that Spontaneously Acquire Experimental Allergic Encephalomyelitis

Eric T. Ahrens, David H. Laidlaw, Carol Readhead, Celia F. Brosnan, Scott E. Fraser, Russell E. Jacobs

Pathology of fixed spinal cords from transgenic mice with a myelin basic protein (MBP) specific T cell receptor was investigated. These mice spontaneously acquire the demyelinating disease experimental allergic encephalomyelitis (EAE). Several complementary imaging modalities, all on the same tissues, were used to visualize lesions; these included high-field (11.7-T) microscopic diffusion tensor imaging (DTI), T_2^*-weighted imaging, and optical microscopy on histological sections. Lesions were predominantly in white matter around meninges and vasculature and appeared hyperintense in anatomical images. DTIs showed reduced diffusion anisotropy in the same hyperintense regions, consistent with inflammation and edema. Histology in the same tissues exhibited the characteristic pathology of EAE. Two techniques for visualizing the effective diffusion tensor fields are presented, which display direction, organization, and integrity of neuronal fibers. It is shown that DTI offers intriguing possibilities for visualizing axonal organization and lesions within white matter.

Key words: transgenic; EAE; diffusion tensor; demyelination.

INTRODUCTION

The recent proliferation of transgenic animal models of human diseases is a major driving force for the development of noninvasive tools for the longitudinal study of mouse pathogenesis. High-field microscopic MRI (μMRI) is well suited for such studies because of its compatibility with *in vivo* investigations, high spatial resolution, and sensitivity to a wide variety of pathological states. In this paper, we report initial μMRI studies of spinal cords in a strain of transgenic mice that express a myelin basic protein-specific T cell receptor (1). These mice spontaneously acquire experimental allergic encephalomyelitis (EAE), which is considered an animal model for the human demyelinating autoimmune disease multiple sclerosis (MS). EAE is characterized by relapsing weakness, paralysis, and eventual death. The histopathology of EAE reveals the presence of inflammatory infiltrates—mostly T cells, B cells, and macrophages, in white matter, meninges, and perivascular regions. EAE lesions contain regions of demyelination with, for the most part, preservation of axons. In most EAE studies, animals of particular haplotypes are experimentally induced to undergo a demyelinating autoimmune attack by inoculation with emulsified crude myelin extracts or purified myelin proteins, such as myelin basic protein (MBP) (for reviews, see refs. 2 and 3).

Recently, a transgenic mouse model of EAE has been constructed that spontaneously acquires the disease in certain environments without the need for inoculation (1). A surprising aspect of these animals is that disease onset varies with their housing. When housed in some animal facilities, they do not acquire disease symptoms unless they are immunized with MBP (1). Mice housed in other facilities, such as the Cedars-Sinai animal facility, acquired the disease spontaneously with an incidence of 100%. This implies that an unidentified environmental factor, perhaps viral, present in some facilities is sufficient to trigger disease onset. The spontaneous triggering of the disease makes these transgenic animals seem to be a closer model to human MS and offers the intriguing possibility that the environmental factor initiating the animal model disease could be identified.

MRI is a sensitive technique for visualizing EAE lesions in a variety of animal models (4–18) and has provided both insight into the mechanisms of the disease and a noninvasive means for monitoring the course of various therapies (4, 8, 9). A number of mechanisms lead to lesion contrast. An increase in the T_2 relaxation time (13, 15, 16) has been reported within white matter lesions and is consistent with the presence of inflammation, demyelination, and edema. Consequently, in T_2-weighted images, lesions appear hyperintense. In addition, T_1 has been reported to increase within lesions (15, 16). The use of extrinsic intravenous contrast media, such as Gd-DTPA, has also been used by several groups (4, 6, 10, 13, 17) as a means to elucidate regions of breakdown in the blood-brain barrier.

Diffusion imaging has also been used to elucidate EAE lesions. Previous studies have used either diffusion-weighted images (DWIs) (14) or measurements of apparent diffusion coefficients (ADCs) along a limited number of directions (5). In DWIs, diffusion-sensitization gradients are applied along one or more directions to impart additional image contrast on the basis of local differences in water diffusion anisotropy and diffusion rate. (A review of these imaging methods is given in ref. 19.) Heide *et al.* (14) observed changes in DWIs on or before the day lesions became apparent in T_2-weighted images. In addition, anomalies in DWIs were observed that were not accompanied by T_2-weighted features. This suggests that DWIs are sensitive to pathological features that do not

MRM 40:119–132 (1998)

From the Beckman Institute and Division of Biology, California Institute of Technology, Pasadena, California (E.T.A., D.H.L., S.E.F., R.E.J.); Cedars-Sinai Medical Center, Los Angeles, California (C.R.); and Albert Einstein College of Medicine, Bronx, New York (C.F.B.).

Address correspondence to: Dr. Eric T. Ahrens, Division of Biology, Caltech, Mail Code 139-74, Pasadena, CA 91125. e-mail: eta@druggist.gg.caltech.edu.

Received June 2, 1997; revised January 5, 1998; accepted January 6, 1998.

This work is supported, in part, by the Human Brain Project funded jointly by the National Institute on Drug Abuse, the National Institute of Mental Health, and the National Science Foundation, and NSF CCR-96-19649. E.T.A. was supported by Grant F32 NS10384 from the National Institute of Neurological Disorders and Stroke.

0740-3194/98 $3.00

affect T_2. Verhoye *et al.* (5) reported a significant correlation between increased ADCs and clinical score within white matter.

ADCs are essentially one-dimensional diffusion coefficient measurements, along one to three orthogonal directions, of an inherent 3 × 3 tensor quantity. Useful qualitative information can be obtained by these methods. However, as previously pointed out (20, 21), the results of DWIs and the values of ADCs measured along a limited number of directions in anisotropic media do not correspond to any intrinsic physical characteristic of the tissue; instead, the results depend on the details of the experiment, such as the orientation of the tissue with respect to the gradient and the magnet axis.

In this study, we investigate imaging EAE lesions in fixed dorsal columns using several MRI modalities, including three-dimensional (3D) T_2^*-weighted FLASH (22) and quantitative diffusion tensor imaging (DTI) (23, 24). The μMRI results are correlated with detailed neuropathological analysis of the same tissues used in the 3D and diffusion imaging. The combination of μMRI and histology in the same specimens provides insight into how lesion contrast in anatomical and diffusion MRI correlates with the details of autoimmune disease of the central nervous system (CNS).

Unlike previous EAE diffusion studies, the DTI methods used in this study are quantitative, rotationally invariant, and independent of specific hardware configurations. DTI results are independent of magnetic field strength, unlike quantitative T_2 or T_1 measurements. Constructing DTIs involves voxel-by-voxel measurement of the entire effective diffusion tensor. Measurement of both the diagonal and off-diagonal tensor elements is necessary to characterize the diffusion anisotropy in three dimensions, which, in turn, reflects the underlying fiber microstructure. The potential of DTI for visualizing EAE pathology originates from the substantial diffusion anisotropy that exists in white matter fibers of the CNS (25–30). The expectation is that white matter lesions will cause a localized reduction in the diffusion anisotropy, as well as changes in the absolute value of diffusion. Thus, localized diffusion measurements will be a useful marker of EAE pathology. In this paper, we demonstrate that the information contained in DTIs, which previously has been used to make maps of neuronal fiber direction, diffusion anisotropy (25, 31, 32), and organization (20), can also be used to highlight regions of inflammation and demyelination in the transgenic EAE spinal cord. Our results build on previous DTI methodologies (20, 21, 23, 24) by implementing them at true microscopic resolutions and by using them as a tool for studying the pathology of an animal model of an autoimmune disease. These studies set the foundation for future longitudinal *in vivo* studies in this transgenic construct and demonstrate that DTI may offer intriguing new possibilities for visualization of white matter lesions.

MATERIALS

EAE is mediated by antigen-specific class II restricted $CD4^+$ T helper type 1 cells. The primary antigen in EAE seems to be MBP. The MBP epitopes that are recognized by T cells correlate to the mouse major histocompatibility complex (MHC) (33). The dominant MBP epitope in B10.PL mice ($H\text{-}2^u$ haplotype) is contained within the amino-terminal residues 1–11 (34). The T cells recognizing this epitope are restricted to antigen recognition in the context of MHC class $I\text{-}A^u$. The transgenic T cell receptor (TCR), cloned from a B10.PL-derived hybridoma specific for MBP (residues 1–11), is encoded by the rearranged Vβ8.2 and the Vα2.3 T cell receptor genes. The transgenic mice are homozygous for the rearranged Vα2.3, with one copy of the Vβ8.2. All of the splenic T cells express the β chain transgene, and an average of 71% express the α chain transgene (1). In these mice, most thymocytes expressed high levels of the TCR transgenes, and there was preferential expression of $CD4^+$ cells, indicating a positive selection of transgenic T cells (1). The transgenic T cells function as helper cells *in vivo* (1).

The transgenic EAE mice were bred in the Cedars-Sinai animal facility. Animals were housed in microisolator cages inside HEPA-filtered laminar-flow hoods. The cages were changed in a laminar flow work station, and the transgenic mice were changed before other strains. At weaning, 1 cm of tail was biopsied while the mouse was under metafane anesthesia; the genotype of the animal was established using polymerase chain reaction (PCR) with oligonucleotide primers specific for the genes encoding the TCR α and β chains. Animals that were positive for both the α and β TCR transgenes were monitored daily for clinical symptoms of disease.

The clinical symptoms were scored according to the convention: 0, normal; 1, limp tail; 2, paraparesis with a clumsy gait; 3, hindlimb paralysis; 4, hindlimb and forelimb paralysis; 5, moribund. The rate of disease progression is animal specific. From past experience, by the end of 4–5 months, most animals develop spontaneous paralysis (stage 3).

A total of 11 mice were imaged in this study. From these, portions of the spinal cord from four stage 3 transgenic mice were investigated, as well as four wild-type B10.PL $H\text{-}2^u$ control rodents. One transgenic animal from each stage 0, 1, and 2 was also investigated. The wild-type mice were all approximately 2 months of age and age-matched to within 2 weeks.

The fixation procedure was as follows: the mouse was first anesthetized with Avertin (0.017 ml/g body weight) and perfused through the left ventricle with Trump's fixative (4% paraformaldehyde, 1% glutaraldehyde, in 0.1 *M* phosphate buffer, pH 7.4). The intact vertebral column was excised, placed into fixative, and stored at 4°C until imaging. The spinal cords used in the diffusion experiments were stored in fixative at 4°C for 36 hours before imaging.

Immediately before imaging, a segment of intact dorsal column in lumbar region L1 through L3 was isolated, rinsed in phosphate-buffered solution (PBS), and sealed in a 5-mm quartz tube for imaging.

METHODS

Instrumentation

μMR images were acquired using a Bruker AMX500 (Bruker Instruments Inc., Billerica, MA) micro-imaging system with a wide-bore (89-mm) 11.7-T magnet, a labo-

ratory-built 5-mm solenoid RF probe, a laboratory-built low-noise preamplifier, and an Acustar (Bruker Instruments Inc., Fremont, CA) shielded gradient coil with a maximum gradient strength of 290 G/cm. The sample was maintained at a temperature of 8°C to ensure the stability of the chemical properties of the tissue over the extended acquisition time required for the DTI experiments. Image visualization was performed on a SGI Indigo workstation (Silicon Graphics Inc., Mountain View, CA) using either VoxelView (Vital Images Inc., Fairfield, IA) or AVS (AVS Inc., Waltham, MA) software. The diffusion tensor results were computed using a HP9000/755 workstation (Hewlett Packard Inc., Palo Alto, CA).

Imaging

Three-dimensional image data were acquired using a 3D variant of the spoiled FLASH (22) protocol with TR = 100 ms, TE = 6 or 7 ms, 512 × 256 × 256 image points, and 30-μm isotropic voxels. The RF excitation pulse angle was optimized to give the approximate Ernst-angle condition (35). In the 3D images, contrast between gray and white matter is presumed to be due to differences in T_2^* between tissues.

The first step toward constructing DTIs was to acquire a series of diffusion-weighted images. These were acquired using a multislice 2DFT protocol with two identical trapezoidal diffusion-sensitizing gradient pulses applied symmetrically before and after the 180° pulse (19, 36). The read compensation and phasing gradient pulses were placed immediately before the readout gradient to minimize the effects of background gradients (37). Diffusion gradient pulses were applied along a total of seven directions. These included the laboratory coordinate directions: (1, 0, 0), (0, 1, 0), and (0, 0, 1), and tetrahedral (38, 39) directions: (1, 1, 1), (−1, −1, 1), (1, −1, −1), and (−1, 1, −1). Along each gradient direction, four values of the so-called diffusion-weighting b matrix (19) were used, with the maximum matrix element of order of 2000 s/mm^2. (Details concerning the evaluation of the b matrices and the calculation of the effective diffusion tensors are discussed below in the Results and Analysis section.) In addition, one image was acquired both at the onset and at the end of the experimental run with the diffusion gradients set to zero; thus, 30 images total were used to obtain the effective diffusion tensors. The gradient pulse timings were fixed at a width of δ = 2 ms and a separation of Δ = 7.4 ms. Multislice data were acquired through the L2 vertebrae with 256 × 256 image points, 20 × 20 μm in-plane resolution, 300-μm-thick slices, and TR/TE = 2000/17 ms.

The DTI protocol was tested on a water phantom, for which diffusion coefficients are accurately known (2.30×10^{-3} mm^2/s at 25.2°C) (40). This was done to estimate the accuracy of the diffusion measurements in our imaging system and to rigorously test for systematic computational errors, background gradients, and other hardware imperfections. The results in water yield diffusion coefficient values (given by the diagonal elements of the diffusion tensor) in agreement with known values to within 5%; the off-diagonal tensor elements were statistically indistinguishable from zero, as expected for the isotropic diffusion case.

Histology

From selected spinal cords used in the imaging experiments, a series of stained histological sections were prepared. These were used for pathological analysis using optical microscopy and for comparisons with the corresponding μMRI "sections." After imaging, the spinal cords were removed from the vertebral bone, dehydrated through a graded series of ethanol concentrations, cleared in propylene oxide, and embedded in Epon 812 epoxy (Ted Pella Inc., Redding, CA). Transverse sections (1 μm thick) were cut, mounted on glass slides, and stained with toluidine blue.

RESULTS AND ANALYSIS

Anatomical Image Results

Anatomical μMR images from the lumbar region of the spinal cord are displayed in Figs. 1A, 1B, 1D, and Figs. 2A through 2D for wild-type and stage 3 transgenic mice, respectively. In addition, Figs. 1C and 2E show corresponding toluidine blue-stained histology sections taken from the same spinal cords used to obtain the MR results. Volume-rendered 3D FLASH data along the transverse plane are shown in Figs. 1A and 1B. Alternate longitudinal views through several vertebrae from the 3D data are also shown in Figs. 1D and 2B. Two-dimensional "I_0" images, which were calculated from a series of diffusion-weighted spin-echo images, are displayed in Figs. 1B and 2D. In I_0 images, contrast is due to differences in T_2 and spin density only. Additional details concerning the calculation of I_0 images are described below.

In both the 2D and 3D images, a large amount of anatomical detail and good contrast among gray matter, white matter, and spinal nerves are observed. Several cytoarchitectonic regions of gray matter can be distinguished, such as the boundary surrounding lamina 10 (Figs. 1A and 1B). Many of the thin fluid-filled subarachnoid spaces surrounding various spinal nerve fasciculi and the meningeal boundary can be resolved and appear hyperintense. Due to the large amount of symmetry in the spinal column, the anatomical structures within voxels in the 300-μm-thick I_0 images are essentially homogeneous.

In the diseased spinal cords, lesions are clearly identifiable (Figs. 2A through 2D) within and surrounding white matter and appear as regions of hyperintensity; this is consistent with the presence of demyelination, inflammatory infiltrates, vasodilation, and edema. Lesions appear primarily near the ventral median fissure, ventral column, meningeal lining, major spinal vessels, and, to a much lesser extent, in the dorsal median septum and dorsal column. A total of four stage 3 transgenic mice were investigated using T_2^*-weighted μMRI. All stage 3 animals showed a substantial lesion load within white matter. However, variability in the degree to which lesions are focal was observed. This can be seen by comparing Figs. 2A and 2D; Fig. 2A shows more localized lesions, especially in the ventral median fissure. As can

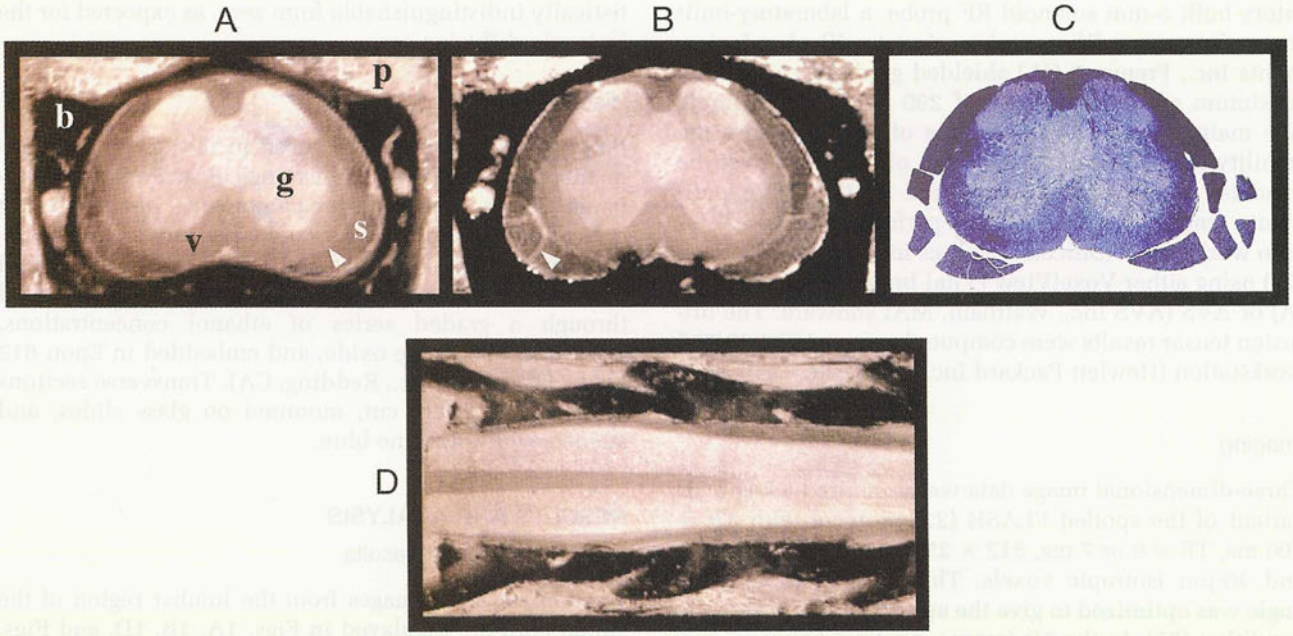

FIG. 1. Images using several imaging modalities. All were acquired in the lumbar region of the same wild-type spinal cord. (A) A volume-rendered transverse image obtained using 3D FLASH with T_2^* weighting, TR = 100 ms, TE = 6 ms, and 30 μm isotropic resolution. (B) A T_2-weighted I_0 spin-echo image calculated from the 2D diffusion-weighted images with TR = 2000 ms, TE = 17 ms, and 20 × 20 × 300 μm resolution. (C) A 1-μm-thick epoxy histology section stained with toluidine blue. (D) An alternate view from the same data as in (A) showing several vertebrae in cross section. In (A), various anatomical regions are shown, including trabecula bone (b), ventral column white matter (v), gray matter (g), spinal cord boundary (arrowhead), spinal nerves (s), and PBS (p) inside the capillary tube surrounding the vertebral segment. In (B), the arrowhead points to a hyperintense subarachnoid space outside the spinal cord.

be seen in Fig. 2B, many lesions extend a substantial distance along the spinal axis, and therefore, most lesions are relatively homogeneous throughout the 300-μm-thick slices used in our tensor imaging. For example, a narrow hyperintense lesion located in the ventral median fissure can be seen in Fig. 2B (arrowhead) extending almost the entire length of the panel (approximately 6.5 mm in length). In the 2D images, the extent and nature of lesions were very similar in different slices in the same animal within the spinal cord regions investigated.

Diseased animals show a less well-defined gray/white matter boundary compared to the wild-type. The regions surrounding the spinal nerves within the vertebral canal seem to be affected by the disease as well (Figs. 2A through 2D), although not by the nerves themselves. Note that a significant enlargement in volume of the subarachnoid cavities, indicated by increased regions of hyperintensity around spinal nerves, is observed.

Histopathology

Histopathological analysis was performed on the same spinal cords used for the anatomical μMRI and DTI results. This allowed us to make a one-to-one correspondence between lesions observed in μMRI and those observed in histological sections. Low-power images are shown in Figs. 1C and 2E. Higher magnification pictures of these same areas are shown in Fig. 3. As can be seen in Figs. 2C through 2E, correlation is found between lesions detected by μMRI and histology. The lesions are predominantly submeningeal in distribution and located in myelinated areas of the cord, particularly involving the ventral columns and associated root-entry zones. Small focal areas of inflammation are also frequently noted around the lateral and dorsal veins. At higher power (Fig. 3B), the lesions can be seen to be composed of perivascular accumulations of lymphocytes and monocytes, with a few scattered polymorphonuclear cells in the leptomeninges, with infiltration of inflammatory cells into the adjacent cord parenchyma. In these regions, there is vacuolation and loss of myelin, with phagocytosis of myelin debris by activated macrophages, and a reactive astrogliosis. In areas of intense inflammation, evidence of Wallerian degeneration can be observed, as indicated by the presence of myelin ovoids. Vasodilation of inflamed veins is predominant, and proteinaceous edema is frequently noted, particularly around veins within the anterior fissure. In contrast to these changes observed within CNS tissues, the adjacent peripheral nerve roots are rarely involved and show only a few scattered inflammatory infiltrates and demyelinated axons.

In tissues sampled at varying times in the disease process, the extent of pathology correlates with the extent of clinical involvement. In animals with no clinical signs, evidence of inflammation and demyelination in the cord is rare. However, as the disease progresses, the number and intensity of the inflammatory foci increase to form a wide rim of inflammation and myelin loss, particularly in the ventral regions of the cord. As the disease becomes more chronic, the number of inflammatory cells gradually wanes, but the extent of Wallerian degeneration and axonal loss is more pronounced. It is interesting that areas of remyelination, as well as areas of active inflammation, can also be found in these later stages (data not shown). The pathology of these lesions is typical of that

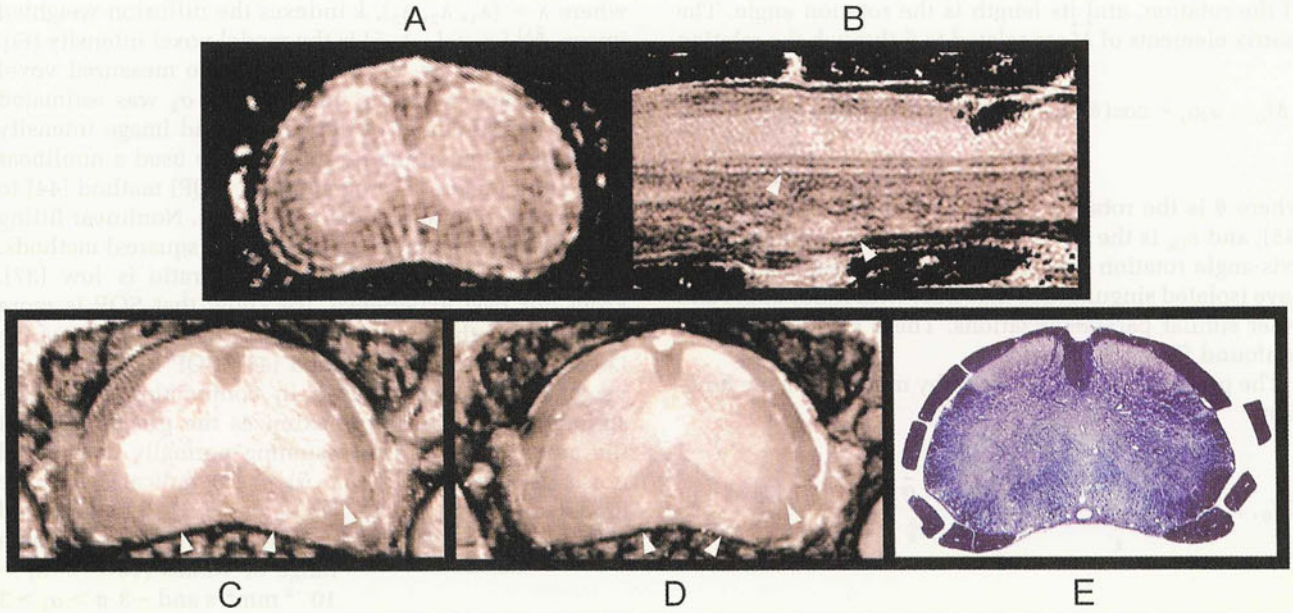

FIG. 2. Images from two different stage 3 transgenic animals in the lumbar region: (A) and (B) show transverse and oblique slices, respectively, from 3D FLASH data with TR = 100 ms, TE = 7 ms, and 30 μm isotropic voxels. Lesions appear as regions of hyperintensity in white matter, and several lesions are pointed to using arrows. In (B), the narrow hyperintense line (top arrowhead) extending the length of the image is the ventral median fissure. Panels (C) through (E) show comparable image slices in a different spinal cord that were obtained using various imaging methods. (C) shows a volume-rendered 3D FLASH image with T_2^* weighting, TR = 100 ms, TE = 6 ms, and 30 μm isotropic resolution. (D) shows an I_0 spin-echo image calculated from the 2D diffusion-weighted images with TR = 2000 ms, TE = 17 ms, and 20 × 20 × 300 μm resolution. (E) shows a 1-μm-thick epoxy histology section stained with toluidine blue. Note that spinal cord (A) exhibits more localized lesions, especially in the ventral median fissure, than (C) (arrowheads) and demonstrates the variability that exists in the lesion distribution among the stage 3 animals.

found in MBP-induced EAE in the wild-type SJL/J mouse, in which severe disease can be induced (41). No evidence was obtained that the expression of the transgenic T cell receptor altered either the pathology or the distribution of EAE lesions within the cerebrospinal axis.

DTI—Analysis

To further investigate the spinal cord microstructure using μMRI, we acquired a series of diffusion-weighted images in diseased and wild-type spinal cords. From these, we computed second-order tensor fields describing the effective rate of water diffusion for each voxel located at coordinates (x, y) within the 2D slices. Each diffusion-weighted image is indexed by k. We assume that the diffusion tensor, $\overleftrightarrow{D}$, with elements D_{ij}, can be related to the measured voxel intensity, $I^{(k)}(x, y)$, of image k, using the model intensity, $\tilde{I}^{(k)}(x, y)$. The model is given by (24)

$$\tilde{I}^{(k)}(x, y) = I_0(x, y)\exp\Big(-\sum_{i=1}^{3}\sum_{j=1}^{3} b_{ij}^{(k)} D_{ij}\Big) \qquad [1]$$

where $I_0(x, y)$ represents the voxel intensity in the absence of diffusion weighting and is treated as an unknown (fit) parameter, and $b_{ij}^{(k)}$ is an element of the diffusion-weighting matrix.

The b matrix parameterizes the amount of diffusion sensitivity applied to an image due to magnetic field gradients. It is calculated from the known time-dependent gradient function, $G_i^{(k)}(t)$, which contains contributions from both the diffusion and imaging gradients. The elements of the b matrix are given by (24, 42)

$$b_{ij}^{(k)} = \gamma^2 \int_{t_0}^{TE} F_i^{(k)}(t)\, F_j^{(k)}(t)\, dt \qquad [2a]$$

and

$$F_i^{(k)}(t) = \int_{t_0}^{t} G_i^{(k)}(t')\, dt' \qquad [2b]$$

where γ is the proton gyromagnetic ratio and t_0 is the time immediately after spin excitation. In Eq. [2b], the sign of $G_i^{(k)}$ is reversed for all gradients after the 180° RF pulse. To solve Eqs. [2a] and [2b], we formulated the integrals as ordinary differential equations; for example, Eq. [2b] can be written as

$$\frac{dF_i^{(k)}(t)}{dt} = G_i^{(k)}(t)\, dt; \quad F_i^{(k)}(t_0) = 0 \qquad [3]$$

and used Runge Kutta (43) and Adams methods (44) to calculate Eqs. [2a] and [2b], respectively.

A total of seven fit parameters from Eq. [1] were obtained, including $I_0(x, y)$ and six other parameters representing the six degrees of freedom of the symmetric second-order tensor $\overleftrightarrow{D}$. We parameterized $\overleftrightarrow{D}$ using the three eigenvalues, λ_1, λ_2, and λ_3; and a vector parameter, $\vec{\alpha}$, which parameterizes the matrix $\overleftrightarrow{M}$ describing the rotation of $\overleftrightarrow{D}$ to the eigenbasis. The direction of $\vec{\alpha}$ is the axis

of the rotation, and its length is the rotation angle. The matrix elements of $\overleftrightarrow{M}$ are related to $\vec{\alpha}$ through the relation

$$M_{ij} = \alpha_i\alpha_j + \cos(\theta)(\delta_{ij} - \alpha_i\alpha_j) - \sum_k \sin(\theta)\varepsilon_{ijk}\alpha_k \quad [4]$$

where θ is the rotation angle, δ_{ij} is the Kronecker delta (45), and ε_{ijk} is the Levi-Civita symbol (45). We used the axis-angle rotation parameterization because it does not have isolated singularities that exist with Euler-angle and other similar parameterizations. These singularities can confound fitting routines.

The parameters were obtained by minimizing the function.

$$E(I_0, \vec{\lambda}, \vec{\alpha}) = \frac{1}{k}\sum_k \frac{[\tilde{I}^{(k)}(x, y, I_0, \vec{\lambda}, \vec{\alpha}) - I^{(k)}(x, y)]^2}{\sigma_k^2} \quad [5]$$

where $\vec{\lambda} = (\lambda_1, \lambda_2, \lambda_3)$, k indexes the diffusion-weighted image, $\tilde{I}^{(k)}(x, y, I_0, \vec{\lambda}, \vec{\alpha})$ is the model voxel intensity (Eq. [1]) at position (x, y), $I^{(k)}(x, y)$ is the measured voxel intensity, and σ_k is the image noise. σ_k was estimated from a measurement of the background image intensity in a region containing no protons. We used a nonlinear sequential quadratic programming (SQP) method (44) to obtain the optimum model parameters. Nonlinear fitting methods are preferable to linear (least squares) methods, especially when the signal-to-noise ratio is low (37). From our past experience, we know that SQP is more robust than other nonlinear fitting routines, such as the Levenburg Marquardt method (43). SQP has rapid convergence and can be used in conjunction with constraints. This algorithm maximizes the probability that the model fits the data assuming normally distributed noise. A fit where $E(I_0, \vec{\lambda}, \vec{\alpha}) = 1.0$ indicates that the model described by Eq. [1] agrees with the measured signal and noise. We constrained $\vec{\lambda}$ and $\vec{\alpha}$ to a reasonable range of values ($10^{-7} > \lambda_i > 10^{-2}$ mm^2/s and $-3\,\pi > \alpha_i > 3\,\pi$). We typically obtained $E(I_0, \vec{\lambda}, \vec{\alpha})$ values in the range of 0.3–1.3, which is near unity, and indicated that our model, including the noise estimates, were reasonable.

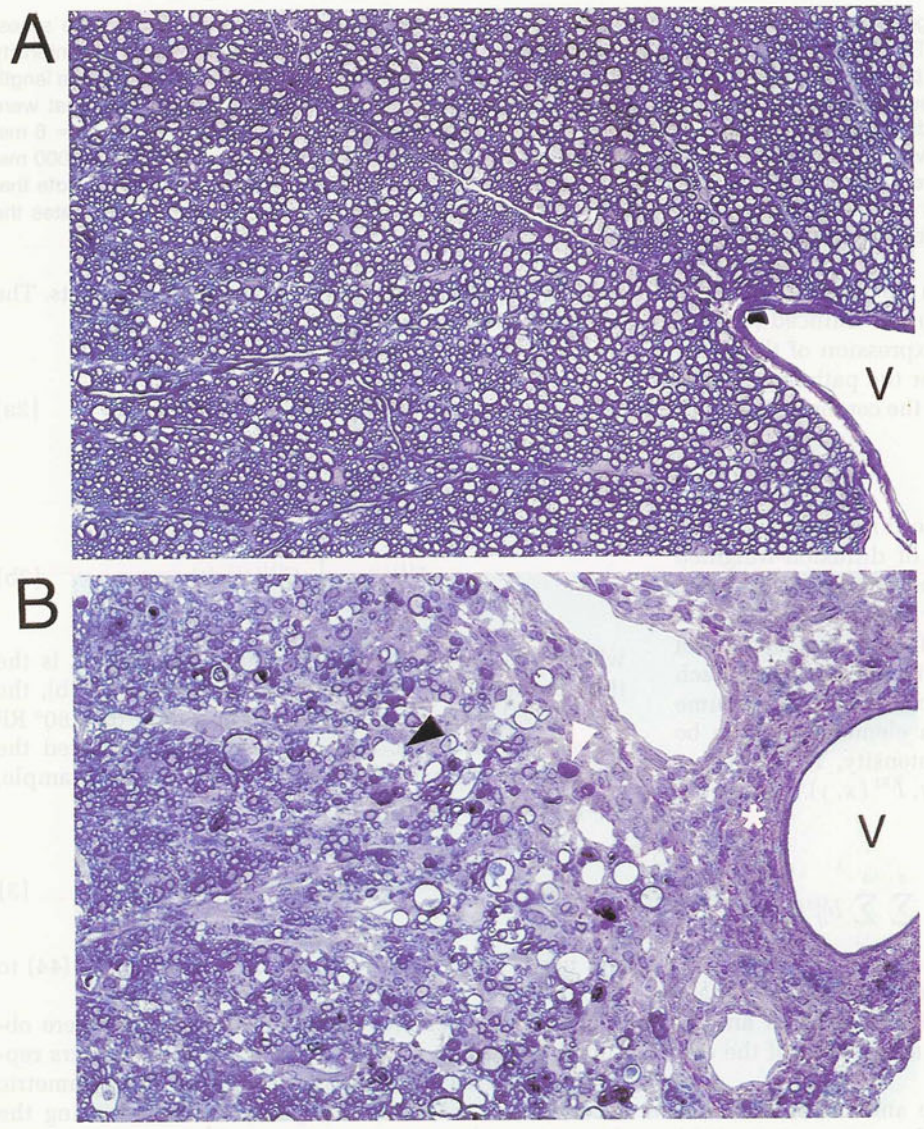

FIG. 3. High magnification views of the wild-type and EAE histological slices from Figs. 1C and 2E, respectively. In this figure, the ventral spinal vessel is shown (V). In (B), regions of perivascular inflammation (asterisk), a myelin ovoid (black arrow), and a vacuole (white arrow) are indicated.

DTI—Results

Visualization of fiber tracts, as well as measurement of their effective diffusion properties, requires knowledge of the diffusion tensor eigenvalues (principal diffusivities, λ_i) and eigenvectors (principal directions) (23). Images showing representative data of the measured voxelwise principal diffusivities for wild-type and stage 3 EAE spinal cords are displayed in Fig. 4. These data are from the same 2D slices shown in the I_0 images of Figs. 1B and 2D. In Fig. 4, the grayscale is calibrated in units of diffusion (mm^2/s). The eigenvalue images show that diffusion within gray matter is approximately isotropic; this is indicated by the similarity in grayscale values within these regions. On the other hand, white matter and spinal nerves exhibit a significant amount of diffusion anisotropy. This is readily seen by comparing regions of fiber tracts in the λ_1 image; these show an increased intensity and, thus, more rapid diffusion along

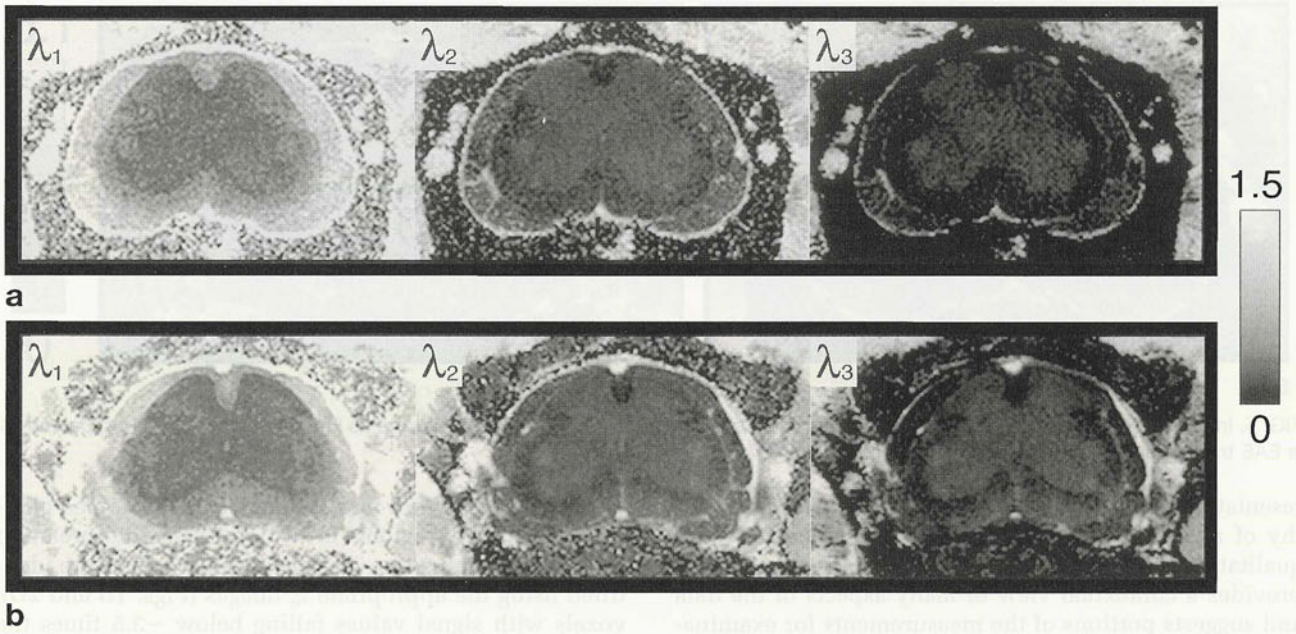

FIG. 4. Images of eigenvalues, λ_1, λ_2, and λ_3 from wild-type (A) and EAE (B) spinal cords. The I_0 images associated with these are displayed in Figs. 1B and 2D. The scale bar, in units of 10^{-3} mm^2/s, relates the image intensity to diffusion values.

this principal direction, compared to similar regions in the λ_2 and λ_3 images.

In Fig. 5, images of the average of the diagonal tensor elements, or $\langle\overleftrightarrow{D}\rangle = 1/3\text{Trace}(\overleftrightarrow{D})$, are shown. This scalar quantity provides a rotationally invariant measure of the directionally averaged diffusion rate of the tissue. In these images, only a small amount of contrast exists among gray matter, white matter, and lesions, indicating a similarity in $\langle\overleftrightarrow{D}\rangle$ values in these regions; thus, our preliminary results in the stage 3 mouse suggests that $\langle\overleftrightarrow{D}\rangle$ is not a particularly sensitive marker of EAE pathology. However, this point must be further investigated in additional animals and stages. We note that the similarity in contrast between gray and white matter has been observed previously in the normal adult cat brain (46) and human brain (47).

Within various regions of interest (ROIs), we calculated mean values of several scalar contractions of the diffusion tensor, including the anisotropy index (AI), defined as $2\lambda_1/(\lambda_2 + \lambda_3)$, the fractional anisotropy (FA) index (defined by Eq. [6], below), and $\langle\overleftrightarrow{D}\rangle$. Four wild-type mice were measured and analyzed using standard statistical methods (described below) to determine "baseline" diffusion properties in the fixed spinal cord at 8°C. The wild-type mice showed substantial diffusion anisotropy in white matter and spinal nerves. For example, AI values were 9 ± 2, 6 ± 2, and 7 ± 2 in dorsal, lateral, and ventral columns, respectively. The parameter FA equals zero for isotropic media and unity for extremely anisotropic media. FA was 0.9 ± 0.1, 0.8 ± 0.1, and 0.8 ± 0.1 in dorsal, lateral, and ventral columns. The spinal nerves had values comparable to that of white matter, with AI and FA equal to 8 ± 3 and 0.8 ± 0.1, respectively. Gray matter exhibited substantially less diffusion anisotropy; in lamina 7, for example, AI was 1.7 ± 0.2 and FA was 0.4 ± 0.1. As described above, $\langle\overleftrightarrow{D}\rangle$ values showed little variation among various ROIs, including gray and white matter; in these regions, $\langle\overleftrightarrow{D}\rangle$ values were equal to (2.1 ± 0.4) × 10^{-4} mm^2/s (lamina 7) and (2.6 ± 0.4) × 10^{-4} mm^2/s (dorsal column).

The mean values of AI, FA, and $\langle\overleftrightarrow{D}\rangle$ within the ROIs for the four wild-type spinal cords were obtained as follows. Four slices per spinal cord were analyzed; all slices were taken in the lumbar region within a single vertebral segment. Each ROI was defined from clusters of voxels that were manually picked for each slice; ROIs contained approximately 50 voxels. For each of these voxels, the parameters AI, FA, and $\langle\overleftrightarrow{D}\rangle$ were calculated from the eigenvalues. The ROI average was obtained from the mean of the voxel parameter values, and the standard deviation of the mean was calculated. The mean and standard deviation for ROIs of a given anatomical region were averaged over all slices and animals. The error bars on the parameter values cited above are plus or minus the mean standard deviations.

An important observation in the EAE spinal cord (Fig. 4B) is that a substantial reduction in the white matter diffusion anisotropy was observed in the same regions that show hyperintensity in I_0 and T_2^*-weighted images and lesions in histology. Using similarly defined ROIs as described above, the mean AI and FA (averaged over four slices in the same cord) was 2.3 ± 0.2 and 0.5 ± 0.1, respectively, for the ventral column and 3.6 ± 0.8 and 0.6 ± 0.1, respectively, for the lateral column. The dorsal column and gray matter showed little involvement with the disease and had anisotropy values essentially equal to that of wild-type. Unlike the anisotropy index, $\langle\overleftrightarrow{D}\rangle$ varied little within ROIs containing lesions (Fig. 5B). The DTI results for this EAE mouse are clearly anomalous compared to wild-type.

Visualization of Diffusion Tensor Fields

We have investigated new approaches for visualizing diffusion tensor fields in a way that gives intuitive rep-

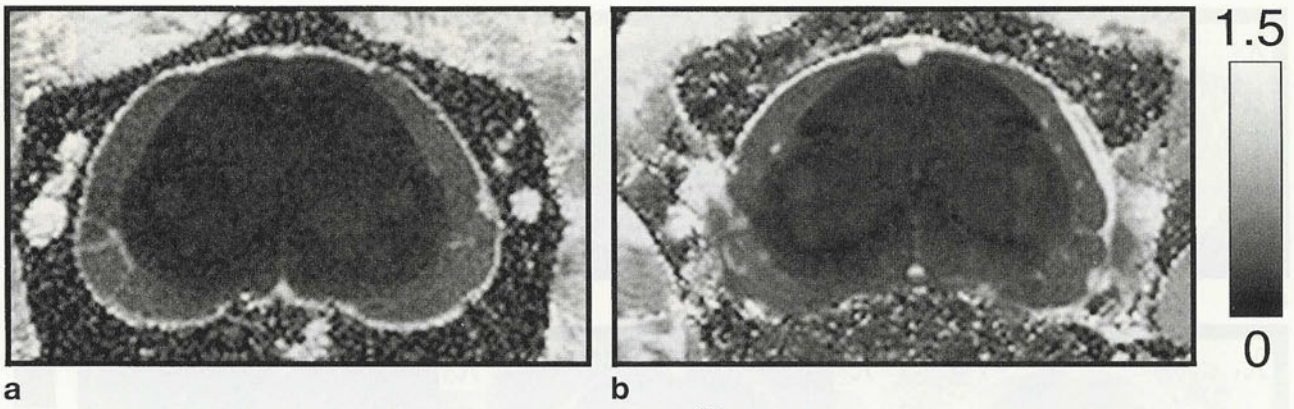

FIG. 5. Images of the average of the diagonal diffusion tensor elements, $\langle \overleftrightarrow{D} \rangle$, from the same data as Fig. 4, where (A) is wild-type and (B) is EAE transgenic. The scale bar is in units of 10^{-3} mm^2/s.

resentations of the direction, organization, and neuropathy of axonal fibers. The visualization process is both qualitative and quantitative. In the qualitative regimen, it provides a contextual view of many aspects of the data and suggests portions of the measurements for examination in further detail. At a quantitative level, a visualization encodes selected aspects of the data into color, intensity, and geometric shape in such a way that the resulting images elucidate the microstructural features of interest and can be easily interpreted by the viewer. Two complementary visualization methods are described below; both use the diffusion data displayed in Fig. 4, and Figs. 1B and 2D show the corresponding I_0 images.

The first method, called the "rice grain" model (Fig. 6), is useful in showing fiber tract direction and organization. Centered in each voxel is a 3D ellipsoid, or rice grain-like object of fixed diameter, the length and orientation of which are a vector quantity. The vector modulus is proportional to FA (20), a unitless, rotationally invariant quantity that is a metric for the amount of anisotropic diffusion ascribed to $\overleftrightarrow{D}$. This quantity is given by (20)

$$\mathrm{FA} = \sqrt{\frac{3}{2}} \frac{\sqrt{\overleftrightarrow{d} : \overleftrightarrow{d}}}{\sqrt{\overleftrightarrow{D} : \overleftrightarrow{D}}} \qquad [6]$$

where

$$\overleftrightarrow{d} : \overleftrightarrow{d} = \sum_{i=1}^{3} \sum_{j=1}^{3} (D_{ij} - \langle \overleftrightarrow{D} \rangle I_{ij})^2 \qquad [7]$$

is the magnitude of the anisotropic part of $\overleftrightarrow{D}$, I_{ij} is an identity matrix element, and

$$\overleftrightarrow{D} : \overleftrightarrow{D} = \sum_{i=1}^{3} \sum_{j=1}^{3} D_{ij}^2 \qquad [8]$$

Note that FA = 0 for $\lambda_1 = \lambda_2 = \lambda_3$ (isotropic system) and that FA = 1 for $\lambda_1 \gg \lambda_2, \lambda_3$. The direction of the rice grain vector is given by the eigenvector $\hat{e}_1$ or the major principal direction of $\overleftrightarrow{D}$ associated with each voxel. In Fig. 6, a filtering algorithm was applied to the tensor fields that removed rice grains (tensors) located in voxels with exceedingly low signal intensity. This helped eliminate grains in regions in which their interpretation would be meaningless. The low-signal voxels were identified using the appropriate I_0 images (Figs. 1B and 2D); voxels with signal values falling below ~3.5 times the mean image intensity over a region containing no protons were eliminated. The resulting array of grains was illuminated by a point light source and tilted at an angle for perspective.

Features of the gross spinal cord anatomy and regions of lesions are shown in Fig. 6. White matter and spinal nerve "fibers" are aligned primarily along the anterior-posterior axis, and gray matter appears more isotropic than does white matter. Regions of lesions (Fig. 6B) show greatly reduced anisotropy (shorter grains) in the same regions that appear hyperintense in the anatomical images, especially around the meningeal boundary, the ventral median fissure, and the ventral columns.

Within various white matter tracts presumed to be uniform, the mean angular deviation in the grain direction was calculated; this provided a measure of the uncertainty in the measured orientation of the grains. Over various ROIs (as defined above), the average of the angular deviation of $\hat{e}_1$ within voxels with respect to a mean ROI $\hat{e}_1$ direction was calculated. Typical mean angular deviations in wild-type white matter are on the order of 1.4° (ventral column).

Most of the grains in the vertebral bone regions were removed after the application of the low-signal filtering algorithm described above. However, many of the remaining grains appear anomalous. This is possibly due to localized susceptibility variations within the trabecular structures that impose magnetic field gradient variations not accounted for in Eq. [2].

The diffusion ellipsoid is a useful tool for representing diffusion in anisotropic media, such as white matter (21, 48). It describes a surface of rotation, oriented by the principal direction axes and scaled by the principal diffusivities. Several authors (20, 25) have constructed diffusion ellipsoid array images. One of the features of this visualization method within heterogeneous systems, such as the CNS, is that there is likely to be a wide range in the magnitude of measured diffusivities (e.g., in gray matter and CSF) and, thus, a wide range in ellipsoid sizes. In this situation, it may be difficult to globally

observe geometric properties, such as eccentricity, of individual or an ensemble of ellipsoids at all locations in the image array at a fixed image magnification.

The second visualization method we describe is the normalized diffusion ellipsoid model. Results of this model are displayed in Fig. 7. It involves placing a diffusion ellipsoid in each image voxel, but with each of the ellipsoid's axes normalized to λ_1. This method is effective in displaying the relative amount of anisotropy in various regions over the entire image. It avoids the "dynamic range" problem encountered when the unnormalized ellipsoids are used. In the normalized ellipsoid model, the size of each ellipsoid remains roughly the same within the array, but changes in shape indicate changes in the directional dependence of diffusion and, thus, tissue microstructure. The drawback to this method is that it throws away information regarding the magnitude of the diffusivities that would be present if the unnormalized ellipsoid were used; one consequence of this is that it is unable to distinguish among regions with different isotropic diffusivities.

In comparing Figs. 7A (wild-type) and 7B (diseased), stark differences in the diffusion anisotropy within white matter can be observed. In wild-type, regions of white matter and spinal nerves appear mostly as prolate ellipsoids oriented along the spinal axis, whereas regions of lesions exhibit greatly reduced anisotropy; thus, the ellipsoids appear more spherical. Both the rice grain and normalized diffusion ellipsoid visualization methods provide intuitive graphical representations of the diffusion anisotropy results presented in the ROI analysis described above. In Fig. 7, a filtering algorithm was used, similar to what was used for the rice grain model, to eliminate ellipsoids within regions of very low signal intensity. As in Fig. 6, a point light source was used for illumination and the image was tilted at an angle for perspective.

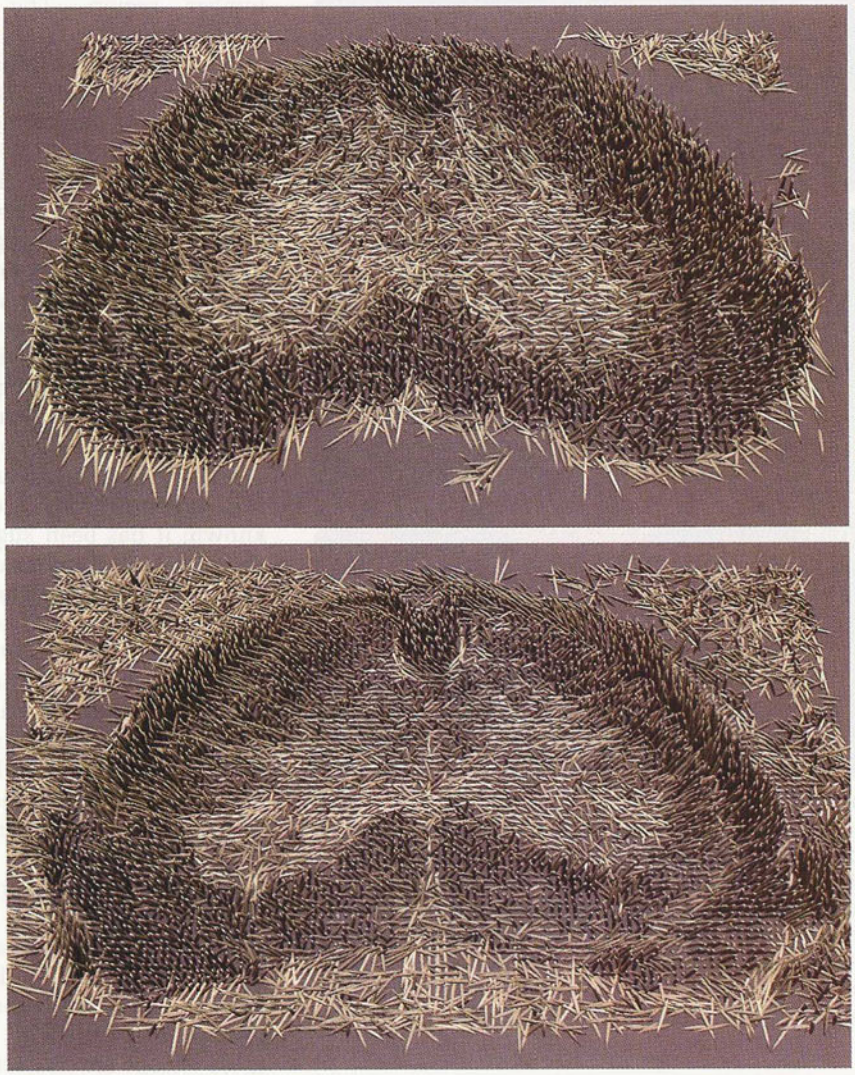

FIG. 6. Rice grain model of effective diffusion tensor data. (A) is wild-type and (B) is stage 3 EAE. This model was generated using the data of Fig. 4, in which Figs. 1B and 2D are the corresponding I_0 images. In each image pixel, a 3D rice grain-like surface is placed, where the length of the grain is normalized to FA and the direction of the grain points along the eigenvector associated with λ_1. The grain width is fixed. A filtering algorithm was applied to remove rice grains in voxels with exceedingly low signal intensity. The array of grains was tilted for perspective and illuminated with a single point light source located above the plane. White matter and spinal nerve grains or "fibers" are aligned primarily along the spinal axis, and gray matter appears more isotropic than does white matter (shorter grains). (B) shows that lesions have reduced anisotropy (shorter grains) in the same regions that appear hyperintense in the anatomical images. For example, note that the lateral boundary between white matter and spinal nerves is more clearly seen in the diseased spinal cord compared to wild-type; this is a consequence of the small FA values along the boundary and indicates a high degree of diffusion isotropy in this region.

DISCUSSION

In this study, we compared several imaging modalities, all applied to the same tissues, to elucidate the pathology of an animal model of an autoimmune disease. The methods used included anatomical μMRI, DTI, and light microscopy from histological preparations; all clearly showed pathological changes associated with the disease. At the qualitative level, both the I_0 and T_2^*-weighted images exhibited similar contrast between lesions and normal white matter. The 2D I_0 images are the prefactors of Eq. [1], and consequently, image contrast is due to differences in T_2 and spin density only; diffusion-weighted contrast, even from the presence of the imag-

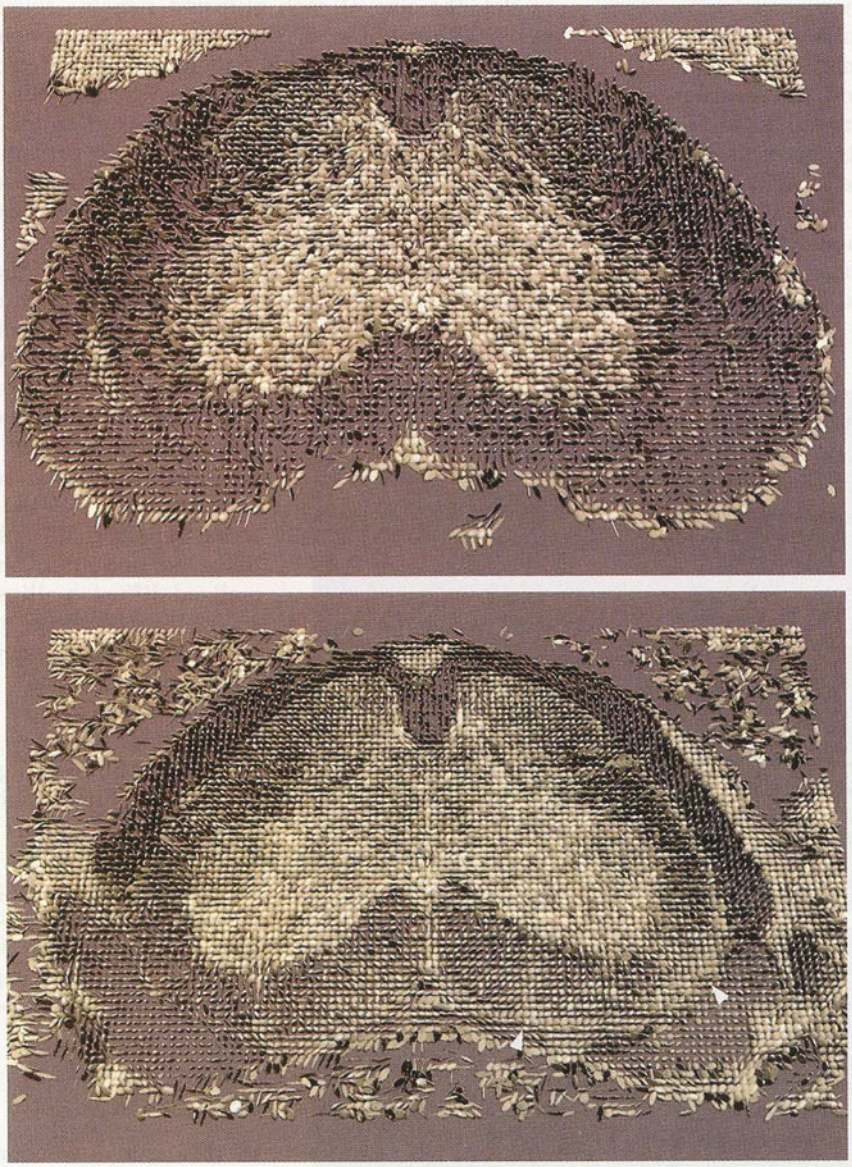

FIG. 7. Normalized diffusion ellipsoid model for wild-type (A) and EAE (B) spinal cords using the data of Fig. 4. Figs. 1B and 2D are the corresponding I_0 images. In each image pixel, a diffusion ellipsoid surface is placed with the principal diffusivities (eigenvalues) normalized to λ_1. A filtering algorithm was applied to remove ellipsoids located in voxels with exceedingly low signal intensity. The ellipsoid array was tilted for perspective and illuminated with a single point light source located above the plane. In comparing (A) and (B), one observes stark differences in the diffusion anisotropy within white matter. In wild-type, regions of white matter and spinal nerves appear mostly as prolate ellipsoids oriented along the spinal axis, whereas regions of white matter lesions in (B) (arrowheads) exhibit greatly reduced anisotropy; thus, the ellipsoids appear more spherical.

ing gradients, is absent. On the other hand, contrast in the 3D FLASH images contain, in general, contributions from differences in T_2, magnetic susceptibility, T_1, spin density, and diffusion properties among tissues.

The signal-to-noise ratio (SNR) of the I_0 images is substantially higher, by a factor of approximately 2.2, compared to any of the individual diffusion-weighted images used in calculating $\overleftrightarrow{D}$. This is due to noise reduction as a result of using multiple images in calculating $\overleftrightarrow{D}$. In the case of the 3D imaging methods, both spin-echo and gradient-echo (FLASH) methods were initially tried, but the gradient-echo methods were ultimately used for this study because they yielded images of superior SNR per unit time.

In all of the spinal cords investigated, the areas of hyperintensity discerned in μMRI in white matter correlate with areas of inflammation detected in the 1-μm toluidine-blue-stained sections. These lesions show a predilection for ventral white matter tracts of the spinal cord, particularly in the lumbar region. The optic nerves form the only other area of the cerebrospinal axis that shows a similar level of involvement. Interestingly, in other species, the distribution of lesions may differ slightly. For example, in the Lewis rat, although the lumbar region of the cord is again extensively involved, vessels located at the gray/white matter border are particularly heavily inflamed, and submeningeal lesions are not as prominent (49). The reasons why specific areas of the CNS are targeted for inflammation are not known; it has been suggested that lymphatic drainage pathways and the relative levels of MBP expression both contribute to this susceptibility (50). Within these areas, inflammation occurs almost exclusively around veins, consistent with the known susceptibility of the venous bed to inflammatory mediators at other sites (51).

In areas adjacent to the ventral median fissure, the hyperintensity is clearly related to the extent of cellular inflammation and tissue damage. In mice sensitized with MBP, these lesions are characterized by parenchymal infiltration of lymphocytes and macrophages, intramyelinic edema, primary demyelination, and Wallerian degeneration. In the early stages of lesion formation, inflammation is first noted around the pia vasculature, and Wallerian degeneration is not prominent; but as the lesion ages, axonal loss becomes more evident and appears to be directly related to the severity of the inflammatory insult, frequently resulting in white matter atrophy. As noted by others, primary demyelination in EAE induced by MBP is not as prominent as that found after sensitization with whole white matter or other myelin antigens. This observation is believed to

reflect the contribution of antibodies to lipid antigens, as well as the distribution of specific myelin proteins within the myelin sheath (52). In this regard, the EAE lesions observed in the transgenic mice closely resemble those noted in animals sensitized by the passive transfer of MBP-reactive T cells or by direct sensitization with MBP and adjuvants. The only difference noted was in the intensity of the inflammatory infiltrate, which was more extensive in the transgenic model and showed less evidence of repair. However, areas of remyelination were found, indicating that some regulation of the inflammatory events can be activated in these animals.

The reason for the hyperintensity observed in the μMRI at the gray/white matter boundary is not so easily correlated with cellular inflammation. It is possible that the blurring of this boundary reflects the distribution of tissue edema. It is well recognized that edema fluid moves more readily through white matter than gray matter, tending to be disseminated in the latter via the perivascular spaces. The development of edema in the cord is a significant correlate of the clinical expression of the disease and reflects extensive damage to the blood-brain barrier that accompanies the cellular inflammatory events (50).

In the diseased animals, an increase in the volume associated with the subarachnoid space surrounding the spinal nerves is observed (Figs. 2A, 2C, and 2D). This is evident by an increase in size of the hyperintense regions surrounding spinal nerves that corresponds to an increase in fluid volume. Histology shows no involvement of the spinal nerves in the disease. Because the vertebral cavity volume remains constant, this observation may suggest that an atrophy of the spinal cord occurs during the course of the disease, leaving the remaining volume to be filled by fluid.

In EAE cords, the anatomical images show regions of hyperintensity in white matter that indicate the possible presence of inflammation, demyelination, edema, and vasodilation. From the anatomical images alone, it is not possible to distinguish between these different pathologies because all appear hyperintense. However, some of these conditions have a distinct signature in DTI. Naked axons, unlike inflammation and edema, have a significant amount of diffusion anisotropy. This anisotropy has been observed in nonmyelinated (53) and premyelinated (54) axons, for example. A measure of the diffusion anisotropy extracted from the diffusion tensor, such as AI or FA, can provide a marker for the presence of naked (demyelinated) axons. By combining relaxation time-weighted images and DTI, one could, in principal, distinguish between regions containing mostly normal white matter, demyelination, or inflammation/edema. On the qualitative level, this picture is consistent with the experimental findings presented here. Regions showing hyperintensity in the (mostly T_2 weighted) anatomical images also show a substantial decrease in the diffusion anisotropy. Histology in the same tissues shows the primary disease diagnosis to be inflammation/edema. Future work involves devising schemes to make composite image maps that combine relaxation time and diffusion information to "stain" for the relevant pathologies.

How accurate are the results of the diffusion measurements reported here? In heterogeneous, anisotropic systems such as the spinal cord, there are a large number of issues that effect the measurement accuracy of $\overleftrightarrow{D}$. Some of these issues have been reviewed by others (25, 37). Although a quantitative analysis of the precision in our $\overleftrightarrow{D}$ measurements is beyond the scope of this paper, we address a few issues that are specific to this study. The presence of systematic measurement errors due to hardware imperfections, gradient calibration errors, and computational errors was investigated using a water phantom, imaged under comparable experimental conditions and resolution as the spinal cord data. The voxelwise diffusion coefficients obtained were in agreement with known values to within 5%, which is acceptable considering the high resolution (and correspondingly large imaging gradients) used in this study. The diffusion coefficients of the PBS surrounding the spinal cords were also measured *in situ* during the data acquisition and the values obtained were comparable to the value of water to within better than 10%.

The matrix form of Eq. [1] is appropriate for systems exhibiting anisotropic diffusion, which is observed in both myelinated and unmyelinated axonal fibers of the nervous system. Diffusion is also restricted or compartmentalized in these systems; this is evident by spectroscopic observations of multiexponential behavior in plots of the echo amplitude versus b values and a diffusion-time dependence to the measured coefficient (53, 55, 56). We do not attempt a detailed description of restricted diffusion in the spinal cord here; however, in restricted systems, the choice of acquisition parameters can influence the measurement results of the effective diffusion tensor. In these systems, the measured effective diffusion tensor depends on the diffusion time, t_d, which is approximately equal to Δ, the gradient pulse separation time, in the limit of short-duration pulses. Along a given direction, the behavior of a measured tensor element for large t_d approaches an asymptotic value that is sensitive to details of the tissue microstructure, such as the extracellular volume fraction and membrane permeability (57). To investigate whether our $\overleftrightarrow{D}$ measurements are in the asymptotic regime, we repeated measurements in a wild-type spinal cord with values of Δ increased from 7.4 ms to 14 and 21 ms. The elements of $\overleftrightarrow{D}$ did not vary significantly for these values, indicating that the data used in this study acquired at Δ = 7.4 ms can be considered in the asymptotic regime.

Ultimately, measurement precision of a diffusion tensor originates from ubiquitous limitations on the experimentally achievable image SNR. SNR considerations limit the choice of the maximum b values used for the diffusion-weighted images. The lower limit of the SNR that is acceptable for diffusion-weighted images used for fitting the DTIs has not been rigorously established, but in our experiments, all of the diffusion-weighted images had a SNR > 2 in ROIs. This arbitrary criterion limited the magnitude of b values to less than ~2000 s/mm^2. Generally, the use of small-magnitude b values (compared to the inverse of the diffusion rate of interest) leads to a reduction in the measurement accuracy of the slower diffusion tensor elements. This point is particularly rel-

evant for clinical imaging systems, in which gradient strength is often limited (47). In our experimental arrangement, the slower tensor components were the off-diagonal elements because most fibers were aligned along the D_{zz} direction.

The presence of image noise can also result in eigenvalue repulsion (58). This statistical biasing effect, which is investigated in ref. 25, tends to make anisotropic material appear even more anisotropic and isotropic material appear anisotropic; as the SNR decreases, this effect intensifies. This effect is likely to bias the results in the ROI analysis slightly so that the metrics of anisotropy are overestimated. In addition, this bias may contribute to the small amount of anisotropy measured in gray matter. For example, in wild-type lamina 7, we obtained AI and FA values equal to 1.7 ± 0.2 and 0.4 ± 0.1, respectively; ideally, in isotropic media, these values should be the equal to 1 and 0. (It is conceivable that a small amount of intrinsic diffusion anisotropy exists in gray matter regions. This is because a few axons can be observed in gray matter in histological sections, and there may be some preferential anisotropic stacking arrangement of cell bodies. This point must be investigated further.) Eigenvalue repulsion can also be observed in the eigenvalue images of Fig. 4. One observes a small systematic difference in intensity between the smallest eigenvalue images throughout white matter regions, where $\lambda_2 > \lambda_3$; ideally, these regions should have "axially symmetric" diffusion, with $\lambda_2 = \lambda_3$. This statistical bias also influences our visualizations of the diffusion tensor fields. For instance, in Fig. 6, many of the grains representing gray matter have a finite length, indicating that FA > 0 in those voxels. Also, some of the ellipsoids in Fig. 7 have a somewhat squashed appearance, which indicate either deviations from isotropy or axial symmetry in the case of gray matter or white matter, respectively.

The diffusion properties measured in fixed tissue are likely to differ somewhat from *in vivo* spinal cord results. We emphasize that our goal in this study was to evaluate the potential of MR microscopy to study regional differences in diseased tissue rather than to obtain benchmark *in vivo* results. We are not aware of any direct systematic comparisons between diffusion results in fixed versus *in vivo* CNS tissue. The "transfer function," which scales diffusion measurements made in fixed tissue to appropriate *in vivo* values, is not known. In addition, one expects that relaxation time and diffusion properties may depend on details of the tissue preparation, such as the fixation method, time the tissue is stored in fixative, and temperature history. Gulani *et al.* (59) noted an age-related decrease in diffusion coefficients parallel to white matter tracts in formalin-fixed rat spinal cord over a period of 2 weeks. To investigate a possible storage time dependence of the diffusion properties in our experiments, we remeasured the tensors in a single wild-type cord stored in PBS at 4°C for 1 week after the initial scan. (All spinal cords were stored in fixative for approximately 36 hours at 4°C before imaging.) No significant changes in diffusion properties was observed in this single experiment, suggesting that, at least between 36 hours and 1 week postfixation, the properties remain relatively stable.

Because our diffusion data were acquired at temperatures well below physiological conditions (8°C), the measured diffusion rates are slower than previously published results in CNS tissue. Metrics of anisotropy, however, should be much less temperature dependent and, thus, more suitable for comparisons. Our wild-type measurements of AI in white matter ranged from 6 ± 2 (lateral columns) to 9 ± 2 (dorsal columns). These values are slightly larger than the results of Gulani *et al.* (59), who measured tensor elements along a limited number of directions in the fixed rat spinal cord; they reported 3.9 in lateral columns and 4.7 in dorsal columns. Also, these values are slightly smaller than those reported for white matter in the *in vivo* brain studies of ref. 25 but significantly larger than the values (~3) in ref. 19 (p. 137); in these later comparisons, we assume that one can compare our fixed tissue results with *in vivo* results.

On the basis of our fixed tissue results, an exciting prospect is the use of these μMRI methods for studying the disease *in vivo* and in a longitudinal fashion. This will allow possible early detection of lesions, distinguishing between various white matter pathologies on the basis of MRI measurements alone (i.e., demyelination and inflammation/edema), and evaluation of the efficacy of various therapeutic treatments, just to give a few examples. To obtain DTIs at high spatial resolutions (10–100 μm) *in vivo,* several issues are critical. First, there is the issue of motion, which can cause serious errors when trying to quantify diffusion. Proper experimental design can reduce this problem through the implementation of such methods as stereotactic restraints, cardiorespiratory-gated acquisition, and movement-detecting pulse sequences. Perhaps, a more serious issue is that of imaging time. The acquisition rate of the spin-echo methods used in this study are inherently slow; however, by the use of gradient-echo methods, such as diffusion-sensitized FLASH (22), the acquisition rate can be decreased by at least an order of magnitude. (The implementation of echo-planar methods is problematic at high magnetic field strengths.) Imaging time can also be reduced if one could limit the number of diffusion tensor elements measured. For example, acquisition of only trace images, or $\langle \overleftrightarrow{D} \rangle$, greatly reduces the imaging time; these images are useful in the early diagnosis of brain ischemia (reviewed in ref. 19), and rapid scanning methods exist for the determination of $\langle \overleftrightarrow{D} \rangle$. However, it is observed that $\langle \overleftrightarrow{D} \rangle$ is not a particularly good marker of EAE pathology. This observation has been shared by others (60). Measurement of the diffusion anisotropy is a much better marker, and this requires knowledge of the off-diagonal tensor elements, which, in turn, requires measurement of the entire diffusion tensor and a longer scan time.

SUMMARY AND CONCLUSIONS

In this study, we combined a variety of microscopic MRI methods to elucidate fixed-tissue pathology in an animal model of an autoimmune disease. The μMRI methods are complementary to more conventional histological techniques. In addition, they have the ability to image lesions in 3D and provide microstructural information.

In I_0 and T_2^*-weighted images, EAE lesions appear hyperintense; this is consistent with the presence of demyelination, inflammation, edema, and vasodilation. Histopathological analysis in the same tissues using stained sections reveal the presence of these pathologies; the primary one is perivascular inflammation, at least in the later stages of the disease. Histology also shows evidence of Wallerian degeneration, remyelination, and vacuolation. Overall, the pathology in the transgenic mice with EAE seems similar to that observed in the SJL/J mouse, with disease induced by inoculation with purified MBP and adjuvant or by passive transfer. Within the same tissues, sites of white matter lesions in the μMRI, indicated by regions of hyperintensity, appear to coincide with lesions observed in the stained histological sections.

We show that DTI is a powerful tool for elucidating white matter fiber organization and integrity of neuronal fibers in diseased animals at high spatial resolutions. A significant reduction in the measured diffusion anisotropy is observed in the same white matter regions that show hyperintensity in the anatomical images; this is consistent with the presence of inflammation and edema. In addition, we present two new techniques for the visualization of the diffusion tensor data. These methods are capable of displaying the direction, diffusion anisotropy, and organization of neuronal fibers in an intuitive manner.

ACKNOWLEDGMENTS

The authors thank L. Hood and D. Zaller for initially supplying us with the transgenics; P. Calderon and S. Mehta at Bruker Instruments and J. Edens and D. De Sha at Caltech for helpful technical support. The authors also thank T. Hudspeth and colleagues at Hughes Aircraft for their expertise in preamplifier design and P. T. Narasimhan and P. Mitra for helpful discussions.

REFERENCES

1. J. Goverman, A. Woods, L. Larson, L. P. Weiner, L. Hood, D. M. Zaller, Transgenic mice that express a myelin basic protein-specific T cell receptor develop spontaneous autoimmunity. *Cell* **72,** 551–560 (1993).
2. C. S. Raine, Biology of disease: analysis of autoimmune demyelination: its impact upon multiple sclerosis. *Lab. Invest.* **50,** 608–635 (1984).
3. S. S. Zamvil, L. Steinman, The T lymphocyte in experimental allergic encephalomyelitis. *Annu. Rev. Immunol.* **8,** 579–621 (1990).
4. S. P. Morrissey, R. Deichmann, J. Syha, C. Simonis, U. Zettl, J. J. Archelos, S. Jung, H. Stodal, H. Lassmann, K. V. Toyka, A. Haase, H. P. Hartung, Partial inhibition of AT-EAE by an antibody to ICAM-1-clinico-histological and MRI studies. *J. Neuroimmunol.* **69,** 85–93 (1996).
5. M. R. Verhoye, E. J. s'-Gravenmade, E. R. Raman, J. Van Reempts, A. Van der Linden, In vivo noninvasive determination of abnormal water diffusion in the rat brain studied in an animal model for multiple sclerosis by diffusion-weighted NMR imaging. *Magn. Reson. Imaging* **14,** 521–532 (1996).
6. S. P. Morrissey, H. Stodal, U. Zettl, C. Simmons, S. Jung, R. Kiefer, H. Lassmann, H. P. Hartung, A. Haase, K. V. Toyka, In-vivo MRI and its histological correlates in acute adoptive transfer experimental allergic encephalomyelitis—quantification of inflammation and edema. *Brain* **119,** 239–248 (1996).
7. T. L. Richards, E. C. Alvord, J. Peterson, S. Cosgrove, R. Petersen, K. Petersen, A. C. Heide, J. Cluff, L. M. Rose, Experimental allergic encephalomyelitis in non-human primates—MRI and MRS may predict the type of brain damage. *NMR Biomed.* **8,** 49–58 (1995).
8. C. P. Genain, T. Roberts, R. L. Davis, M. H. Nguyen, A. Uccelli, D. Faulds, Y. Li, J. Hedgpeth, S. L. Hauser, Prevention of autoimmune demyelination in nonhuman-primates by a CAMP-specific phosphodiesterase inhibitor. *Proc. Natl. Acad. Sci. U S A* **92,** 3601–3605 (1995).
9. I. J. Namer, J. Steibel, P. Poulet, Y. Mauss, J. P. Armspach, B. Eclancher, J. Chambron, Hyperbaric-oxygen treatment in acute experimental allergic encephalomyelitis—contribution of magnetic resonance-imaging study. *NeuroImage* **1,** 308–312 (1994).
10. I. J. Namer, J. Steibel, S. J. Piddlesden, M. Mohr, P. Poulet, J. Chambron, Magnetic-resonance-imaging of antibody-mediated demyelinating experimental allergic encephalomyelitis. *J. Neuroimmunol.* **54,** 41–50 (1994).
11. D. Lanens, A. Van der Linden, P. O. Gerrits, E. J. 's-Gravenmade, In vitro NMR micro imaging of the spinal cord of chronic relapsing EAE rats. *Magn. Reson. Imaging* **12,** 469–475 (1994).
12. P. A. Seeldrayers, J. Syha, S. P. Morrissey, H. Stodal, K. Vass, S. Jung, T. Gneiting, H. Lassmann, A. Haase, H. P. Hartung, K. V. Toyka, Magnetic-resonance-imaging investigation of blood-brain-barrier damage in adoptive transfer experimental allergic encephalomyelitis. *J. Neuroimmunol.* **46,** 199–206 (1993).
13. S. J. Karlik, E. A. Grant, D. Lee, J. H. Noseworthy, Gadolinium enhancement in acute and chronic-progressive experimental allergic encephalomyelitis in the guinea-pig. *Magn. Reson. Med.* **30,** 326–331 (1993).
14. A. C. Heide, T. L. Richards, E. C. Alvord, J. Peterson, L. M. Rose, Diffusion imaging of experimental allergic encephalomyelitis. *Magn. Reson. Med.* **29,** 478–484 (1993).
15. I. J. Namer, J. Steibel, P. Poulet, J. P. Armspach, M. Mohr, Y. Mauss, J. Chambron, Blood-brain-barrier breakdown in MBP-specific T-cell induced experimental allergic encephalomyelitis—a quantitative in vivo MRI study. *Brain* **116,** 147–159 (1993).
16. W. A. Stewart, E. C. Alvord, S. Hruby, L. D. Hall, D. W. Paty, Magnetic-resonance-imaging of experimental allergic encephalomyelitis in primates. *Brain* **114,** 1069–1096 (1991).
17. C. P. Hawkins, F. Mackenzie, P. Tofts, E. P. G. H. Doboulay, W. I. Mcdonald, Patterns of blood-brain-barrier breakdown in inflammatory demyelination. *Brain* **114,** 801–810 (1991).
18. S. J. Karlik, J. J. Gilbert, C. Wong, M. K. Vandervoort, J. H. Noseworthy, NMR studies in experimental allergic encephalomyelitis: factors which contribute to T1 and T2 values. *Magn. Reson. Med.* **14,** 1–11 (1990).
19. D. Le Bihan, "Diffusion and Perfusion Magnetic Resonance Imaging—Applications to Functional MRI," Raven Press, New York, 1995.
20. P. J. Basser, C. Pierpaoli, Microstructural and physiological features of tissues elucidated by quantitative-diffusion tensor MRI. *J. Magn. Reson. B* **111,** 209–219 (1996).
21. P. J. Basser, Inferring microstructural features and the physiological state of tissues from diffusion-weighted images. *NMR Biomed.* **8,** 333–344 (1995).
22. A. Haase, Snapshot FLASH MRI. Applications to T1, T2, and chemical shift imaging. *Magn. Reson. Med.* **13,** 77–89 (1990).
23. P. J. Basser, J. Mattiello, D. LeBihan, MR diffusion tensor spectroscopy and imaging. *Biophys. J.* **66,** 259–267 (1994).
24. P. J. Basser, J. Mattiello, D. LeBihan, Estimation of the effective self-diffusion tensor from the NMR spin-echo. *J. Magn. Reson. B* **103,** 247–254 (1994).
25. C. Pierpaoli, P. J. Basser, Toward a quantitative assessment of diffusion anisotropy. *Magn. Reson. Med.* **36,** 893–906 (1996).
26. C. Thompson, O. Henriksen, P. Ring, In vivo measurement of water self diffusion in the human brain by magnetic resonance imaging. *Acta. Radiol. Scand.* **28,** 353–358 (1987).
27. M. E. Moseley, Y. Cohen, J. Kucharczyk, J. Mintorovitch, H. S. Asgari, M. F. Wendland, J. Tsudura, D. Norman, Diffusion-weighted MR imaging of anisotropic water diffusion in cat central nervous system. *Radiology* **176,** 439–445 (1990).
28. M. E. Moseley, J. Kucharczyk, H. S. Asgari, D. Norman, Anisotropy in diffusion-weighted MRI. *Magn. Reson. Med.* **19,** 321–326 (1991).
29. C. T. W. Moonen, J. Pekar, M. H. M. de Vleeschouwer, P. van Gelderen, P. C. M. van Zijl, D. DesPres, Restricted and anisotropic displacement of water in healthy cat brain and in stroke studied by NMR diffusion imaging. *Magn. Reson. Med.* **19,** 327–332 (1991).
30. J. V. Hajnal, M. Doran, A. S. Hall, A. G. Collins, A. Oatridge, J. M. Pennock, I. R. Young, G. M. Bydder, MR imaging of anisotropically restricted diffusion of water in the nervous system: technical, ana-

tomic and pathologic considerations. *J. Comput. Assist. Tomogr.* **15,** 1–18 (1991).
31. A. M. Ulug, O. Bahkt, R. N. Bryan, P. C. M. van Zijl, Mapping of human brain fibers using diffusion tensor imaging, *in* "Proc., ISMRM, 4th Annual Meeting, New York, 1996," p. 1325.
32. C. Pierpaoli, P. Jezzard, P. J. Basser, High-resolution diffusion tensor imaging of the human brain, *in* "Proc., SMR/ESMRMB, Nice, 1995," p. 899.
33. R. Fritz, D. E. McFarlin, Encephalitogenic epitopes of myelin basic protein. *Chem. Immunol.* **46,** 101–108 (1989).
34. S. S. Zamvil, D. J. Mitchell, A. C. Moore, K. Kitamura, L. Steinman, J. Rothbard, T-cell epitope of the autoantigen myelin basic protein that induces encephalomyelitis. *Nature* **324,** 258–260 (1986).
35. P. T. Callaghan, "Principles of Nuclear Resonance Microscopy," Oxford University Press, New York, 1991.
36. E. O. Stejskal, J. E. Tanner, Spin diffusion measurements: spin echos in the presence of a time-dependent field gradient. *J. Chem. Phys.* **42,** 288–292 (1965).
37. T. E. Conturo, R. C. McKinstry, J. A. Aronovitz, J. J. Neil, Diffusion MRI: precision, accuracy and flow effects. *NMR Biomed.* **8,** 307–332 (1995).
38. G. Liu, P. van Gelderen, C. T. W. Moonen, Single shot diffusion MRI on a conventional clinical instrument, *in* "Proc., SMR, 2nd Annual Meeting, San Francisco, 1994," p. 1034.
39. G. Y. Liu, P. van Gelderen, J. Duyn, C. T. W. Moonen, Single-shot diffusion MRI of human brain on a conventional clinical instrument. *Magn. Reson. Med.* **35,** 671–677 (1996).
40. H. Weingartner, Self diffusion in liquid water. A reassessment. *Z. Phys. Chem. (Neue Folge)* **132,** 129–149 (1982).
41. C. S. Raine, F. Mokhtarian, D. E. McFarlin, Adoptively transferred chronic relapsing experimental autoimmune encephalomyelitis in the mouse. *Lab. Invest.* **51,** 534–546 (1984).
42. J. Mattiello, P. J. Basser, D. LeBihan, Analytical expression for the b matrix in NMR diffusion imaging and spectroscopy. *J. Magn. Reson. A* **108,** 131–141 (1994).
43. W. H. Press, S. A. Teukolsky, W. T. Vetterling, B. P. Flannery, "Numerical Recipies in C: The Art of Scientific Computing," Cambridge University Press, New York, 1992.
44. "NAG Fortran Library," Numerical Algorithms Group, Downers Grove, IL, 1993.
45. G. Arfken, "Mathematical Methods for Physicists," Academic Press Inc., Orlando, 1985.
46. P. van Gelderen, M. H. M. de Vleeschouwer, D. DesPres, J. Pekar, P. C. M. van Zijl, C. T. W. Moonen, Water diffusion and acute stroke. *Magn. Reson. Med.* **31,** 154–163 (1994).
47. C. Pierpaoli, P. Jezzard, P. J. Basser, A. Barnett, G. Di Chiro, Diffusion tensor MR imaging of the human brain. *Radiology* **201,** 637–648 (1996).
48. J. Crank, "The Mathematics of Diffusion," Oxford University Press, Oxford, 1975.
49. L. Claudio, Y. Kress, J. Factor, C. F. Brosnan, Mechanisms of edema formation in experimental autoimmune encephalomyelitis. The contribution of inflammatory cells. *Am. J. Pathol.* **137,** 1033 (1990).
50. C. F. Brosnan, L. Claudio, Brain microvasculature and multiple sclerosis, *in* "An Introduction to the Blood-Brain Barrier: Methodology and Biology" (W. M. Partridge, Ed.), Cambridge University Press, Cambridge, in press.
51. J. S. Pober, R. S. Cotran, Overview: the role of endothelial cells in inflammation. *Transplantation* **50,** 537 (1990).
52. C. F. Brosnan, C. S. Raine, Mechanisms of immune injury in multiple sclerosis. *Brain Pathol.* **6,** 243 (1996).
53. C. Beaulieu, P. S. Allen, Determinants of anisotropic water diffusion in nerves. *Magn. Reson. Med.* **31,** 394–400 (1994).
54. D. M. Wimberger, T. P. Roberts, A. J. Barkovich, L. M. Prayer, M. E. Moseley, J. Kucharczyk, Identification of "premyelination" by diffusion-weighted MRI. *J. Comput. Assist. Tomogr.* **19(1),** 28–33 (1995).
55. C. Beaulieu, P. S. Allen, An *in vitro* evaluation of the effects of local magnetic-susceptibility-induced gradients on anisotropic water diffusion in nerve. *Magn. Reson. Med.* **36,** 39–44 (1996).
56. G. J. Stanisz, A. Szafer, G. A. Wright, R. M. Henkelman, An analytical model of restricted diffusion in bovine optic nerve. *Magn. Reson. Med.* **37,** 103–111 (1997).
57. L. L. Latour, K. Svoboda, P. P. Mitra, C. H. Sotak, Time-dependent diffusion of water in a biological model system. *Proc. Natl. Acad. Sci. U S A* **91,** 1229–1233 (1994).
58. M. L. Mehta, "Random Matrices," Academic Press Inc., San Diego, 1991.
59. V. Gulani, H. Jiang, G. A. Iwamoto, P. C. Lauterbur, Rapid diffusion tensor microimaging of excised rat spinal cords, *in* "Proc., ISMRM, 4th Annual Meeting, New York, 1996," p. 1321.
60. M. A. Horsfield, M. Lai, S. L. Webb, G. J. Barker, P. S. Tofts, R. Turner, P. Rudge, D. H. Miller, Apparent diffusion coefficients in benign and secondary progressive multiple sclerosis by nuclear magnetic resonance. *Magn. Reson. Med.* **36,** 393–400 (1996).